Scattering matrices of volcanic ash particles of Mount St. Helens, Redoubt, and Mount Spurr Volcanoes

O. Muñoz,[1] H. Volten,[2,3] J. W. Hovenier,[3] B. Veihelmann,[2] W. J. van der Zande,[2,4] L. B. F. M. Waters,[3] and W. I. Rose[5]

[1] We present measurements of the whole scattering matrix as a function of the scattering angle at a wavelength of 632.8 nm in the scattering angle range 3°–174° of randomly oriented particles taken from seven samples of volcanic ashes corresponding to four different volcanic eruptions: the 18 May 1980 Mount St. Helens eruption, the 1989–1990 Redoubt eruption, and the 18 August and 17 September 1992 Mount Spurr eruptions. The samples were collected at different distances from the vent. The samples studied contain large mass fractions of fine particles and were chosen to represent ash that could remain in the atmosphere for at least hours or days. They include fine ashfall samples that fell at a variety of distances from the volcano and pyroclastic flows that retained their fine fractions. Together, they represent a range of ashes likely to remain in the atmosphere in volcanic clouds following eruptions from convergent plate boundary volcanoes, Earth's most important group of explosive sources of ash. All measured scattering matrix elements are confined to rather limited domains when plotted as functions of the scattering angle following the general trends presented by irregular mineral particles. This similarity in the scattering behavior justifies the construction of an average scattering matrix for volcanic ash particles as a function of the scattering angle. To facilitate the use of the average scattering matrix for multiple-scattering calculations with polarization included, we present a synthetic scattering matrix based on the average scattering matrix for volcanic ashes and the assumption that the diffraction forward scattering peak is the same for randomly oriented nonspherical particles and projected-surface-area-equivalent spheres. This synthetic scattering matrix is normalized so that the average of its 1-1 element over all directions equals unity. It is available in the full range from 0° to 180° and can be used, for example, for interpretation of remote-sensing data after a volcanic eruption when the actual properties of the volcanic ash are not known. The measured results for the Mount St. Helens sample have been compared with results of Lorenz-Mie calculations for projected-surface-area-equivalent spheres with the refractive index of the Mount St. Helens particles. We find strong differences between measured and calculated values. *INDEX TERMS:* 0305 Atmospheric Composition and Structure: Aerosols and particles (0345, 4801); 0343 Atmospheric Composition and Structure: Planetary atmospheres (5405, 5407, 5409, 5704, 5705, 5707); 0360 Atmospheric Composition and Structure: Transmission and scattering of radiation; 0370 Atmospheric Composition and Structure: Volcanic effects (8409); 0933 Exploration Geophysics: Remote sensing; *KEYWORDS:* aerosols and particles, planetary atmospheres, remote sensing

Citation: Muñoz, O., H. Volten, J. W. Hovenier, B. Veihelmann, W. J. van der Zande, L. B. F. M. Waters, and W. I. Rose (2004), Scattering matrices of volcanic ash particles of Mount St. Helens, Redoubt, and Mount Spurr Volcanoes, *J. Geophys. Res.*, *109*, D16201, doi:10.1029/2004JD004684.

[1]Instituto de Astrofísica de Andalucía, Consejo Superior de Investigaciones Científicas, Granada, Spain.

[2]Institute for Atomic and Molecular Physics, Dutch Foundation for Fundamental Research on Matter, Amsterdam, Netherlands.

[3]Astronomical Institute "Anton Pannekoek," University of Amsterdam, Amsterdam, Netherlands.

[4]Department of Molecular and Laser Physics, Faculty of Sciences, University of Nijmegen, Nijmegen, Netherlands.

[5]Department of Geological Engineering and Sciences, Michigan Technological University, Houghton, Michigan, USA.

1. Introduction

[2] Volcanic eruptions inject gas and ash particles into the atmosphere, affecting the climate on Earth. A worldwide effect of volcanoes is the warming of the Earth by some particles and the cooling by other particles, depending on their physical properties, i.e., sizes, colors, and shapes.

[3] Light-scattering properties of volcanic ashes are required in order to study their influence on global climate changes. Volcanic ash particles show a wide variety of irregular shapes and have broad size distributions. This

makes it very difficult, if it is possible at all, to perform a theoretical study of the scattering properties of such particles. Most satellite aerosol retrievals are still based on the Lorenz-Mie theory for spherical particles. However, from experimental [e.g., *West et al.*, 1997; *Muñoz et al.*, 2000, 2001; *Volten et al.*, 2001] and theoretical as well as computational [e.g., *Mischenko et al.*, 1996, 2002; *Krotkov et al.*, 1999; *Dubovik et al.*, 2002] results it has become clear that particle shape is highly important in determining the overall light-scattering behavior of aerosol particles. Unfortunately, theoretical and numerical techniques are not suited for realistic polydispersions of volcanic ash particles, because of their wide ranges of sizes and shapes. Consequently, experimental studies remain an important source of information on scattering properties of irregular ash particles. The experimental data can be used for different purposes. The measured scattering matrices can, for example, be used to evaluate models used to calculate scattering properties of nonspherical particles [see, e.g., *Nousiainen and Vermeulen*, 2003]. Further, the experimental data can be used to estimate how nonsphericity can affect the results of satellite retrievals [*Mishchenko et al.*, 2003].

[4] We have experimentally studied the complete scattering matrices as functions of the scattering angle of seven selected ash samples. The measurements were carried out at 632.8 nm. All of the samples were chosen to represent fine-grained particles that would be expected to have atmospheric residence for periods of at least hours and perhaps days or weeks. Particles coarser than about 1 mm fall out of the atmosphere in ~30 min or less, so we have focused on samples that are finer than the ash studied by many volcanological investigators. The samples we chose include the following: (1) a sample of dacitic pyroclastic flow from the 1989–1990 eruption of Mount St. Helens, Washington; (2) two andesitic samples from the 1989–1990 eruption of Redoubt Volcano, Alaska; (3) two andesitic ashes from the 18 August 1992 eruption of Crater Peak, Mount Spurr, Alaska; and (4) two andesitic ash samples from the 17–18 September 1992 eruption of Crater Peak, Mount Spurr, Alaska. Details of the samples are discussed below in section 3.1. This study is part of an ongoing project that involves a systematic study of the scattering properties of different types of volcanic ashes [*Volten et al.*, 2001; *Muñoz et al.*, 2002]. We also compare our measured results for the Mount St. Helens sample with Lorenz-Mie calculations for spheres with the same projected surface area and refractive index.

[5] The measured scattering matrices for the distinct samples are found to agree well in their overall trends and behavior. This similarity justifies the construction of an average scattering matrix for volcanic ash particles as a function of the scattering angle. The lack of experimental data at very small and very large scattering angles (0°–3° and 174°–180°) limits the direct applicability of the average scattering matrix as a function of the scattering angle in remote sensing. However, the experimental scattering matrices can be extrapolated to cover the entire angle range so that the resulting data can be used for practical applications. We have obtained a synthetic scattering matrix based on the average scattering matrix for volcanic ashes. The "synthetic" scattering matrix is available on the entire interval from 0° to 180° following the procedure given by *Liu et al.* [2003].

[6] In section 2 we present a brief review of the basic scattering concepts and a description of the experimental approach. Section 3 summarizes the physical characteristics of our volcanic ash samples. Results and a discussion of our experiments, comparison with Lorenz-Mie calculations, and the construction of the average and "synthetic" scattering matrix for volcanic ashes are given in section 4. Conclusions are presented in section 5.

2. Setup

[7] The flux and state of polarization of a beam of quasi-monochromatic light can be described by means of a so-called Stokes vector. If light is scattered by a sample of randomly distributed and randomly oriented particles and time reciprocity applies, as is the case in our experiment, the Stokes vectors of the incident beam and scattered beam are related by the 4×4 scattering matrix, for each scattering angle θ, as follows [*van de Hulst*, 1957]:

$$
\begin{pmatrix} I_{sca} \\ Q_{sca} \\ U_{sca} \\ V_{sca} \end{pmatrix} = \frac{\lambda^2}{4\pi^2 D^2} \begin{pmatrix} F_{11} & F_{12} & F_{13} & F_{14} \\ F_{12} & F_{22} & F_{23} & F_{24} \\ -F_{13} & -F_{23} & F_{33} & F_{34} \\ F_{14} & F_{24} & -F_{34} & F_{44} \end{pmatrix} \begin{pmatrix} I_{in} \\ Q_{in} \\ U_{in} \\ V_{in} \end{pmatrix},
$$

(1)

where the first elements of the column vectors are fluxes and the other elements describe the state of polarization of the beams. Furthermore, subscripts "inc" and "sca" refer to the incident and scattered beams, respectively, λ is the wavelength, and D is the distance from the sample to the detector. The scattering plane, i.e., the plane containing the directions of the incident and scattered beams, is the plane of reference for the Stokes vectors [*Hovenier and van der Mee*, 1983]. The matrix **F** with elements $F_{i,j}$ is called the scattering matrix of the sample of randomly distributed and randomly oriented particles. Here it is assumed that the particles are much farther apart than their linear dimensions and that multiple scattering by the particles can be neglected. The scattering matrix contains all scattering properties of the sample. The elements of the scattering matrix are dimensionless and depend on the number and properties of the particles, the wavelength of the radiation, and the direction of the scattered light, which, for randomly oriented particles, is sufficiently described by means of the scattering angle θ. It follows from equation (1) that there are 10 matrix elements to be determined. This number is further reduced in case the scattering sample consists of randomly oriented particles with equal amounts of particles and their mirror particles. The four elements $F_{13}(\theta)$, $F_{14}(\theta)$, $F_{23}(\theta)$, and $F_{24}(\theta)$ are then zero over their entire angle range [*van de Hulst*, 1957]. In our experimental apparatus we use a HeNe laser (632.8 nm, 5 mW) as a light source. Clearly, the scattering matrix can be determined by measuring the Stokes vectors of the scattered light for various Stokes vectors of the

Table 1. List of Ash Samples Studied

Sample	Volcano	Date of Eruption	r_{eff}, μm	v_{eff}
Mount St. Helens	Mount St. Helens	18 May 1980	4.1	9.5
2-1-90-Pit 3A-1 (Red. A[a])	Redoubt	Jan. 1990	4.1	9.7
2-21-90-4 (Red. B[a])	Redoubt	Jan. or Feb. 1990	6.4	7.6
44 Ashton	Crater Peak, Spurr	18 Aug. 1992	2.7	4.9
47 Anchorage	Crater Peak, Spurr	18 Aug. 1992	4.8	8.8
39 Gunsight	Crater Peak, Spurr	17 Sept. 1992	3.5	8.2
33 Stop	Crater Peak, Spurr	17 Sept. 1992	14.4	6.6

[a]Name used in this work.

incident light. The laser light in our experiments passes through a polarizer and an electro-optic modulator. The modulated light is subsequently scattered by an ensemble of randomly oriented particles taken from the sample located in a jet stream produced by an aerosol generator. The particles of a particular sample are brought into the jet stream as follows: A compacted mass of powder is loaded into a cylindrical feed stock reservoir. A piston pushes the powder onto a rotating brush at a certain speed. An airstream carries the aerosol particles off the brush through a tube to a nozzle above the scattering volume. A more detailed description is given by *Hovenier et al.* [2003]. The scattered light may pass through a quarter-wave plate and an analyzer (both optional) and is then detected by a photomultiplier tube that moves in steps along a ring around the ensemble of particles. In this way, a range of scattering angles is covered from 3° (nearly forward scattering) to 174° (nearly backward scattering). Owing to the lack of measurements between 0° and 3° and between 174° and 180° we cannot measure the absolute angular dependence of the phase function. Instead, we normalize all measured phase functions to 1 at 30°. All matrix elements (except F_{11} itself) are normalized to F_{11}; that is, we consider F_{ij}/F_{11}, with $i, j = 1–4$ with the exception of $i = j = 1$. Another photomultiplier is placed at a fixed position and used to correct for fluctuations in the particle stream. We investigated the reliability of the measurements presented in this paper by applying the Cloude coherency test [*Hovenier and van der Mee*, 1996]. We found that for all matrix elements the values measured for scattering

angles from 3° to 174° are in agreement with the Cloude coherency test within the experimental errors. A detailed description of the experimental apparatus used to measure the scattering matrices is given by *Hovenier* [2000]. Results for a wide variety of particles have been published by *Muñoz et al.* [2000, 2001, 2002] and *Volten et al.* [2001].

3. Samples

[8] In this section, we discuss physical characteristics of the volcanic ash particles studied in this paper. In particular, we consider their origin and chemical composition, shapes, size distributions, and refractive indices. In Table 1 we present a description of the samples used in this paper. The meaning of the quantities in the last two columns will be explained in section 3.3.

3.1. Eruptions and Samples

[9] Seven ash samples from three volcanoes were studied. They range in bulk composition from andesite to dacite, and all are complex mixtures of silicate glass (55–80% by mass of the bulk material, and this glass contains 62–77 mass % SiO_2) and crystallized silicate mineral phases including plagioclase feldspar, pyroxenes, and amphibole (dominantly plagioclase feldspar). Compositional data on all these ashes and all their components are extensive in the literature, and basic information is presented in Table 2. In the ash samples examined here we should expect that the same materials would be found, but that the relative proportions of glass in

Table 2. Chemical Compositions for Bulk Samples and Glass (Most Abundant Component) From the Eruptions Studied in This Paper[a]

	Mount St. Helens 1980 Bulk wt %[b]	64% of Bulk Glass wt %[b]	Redoubt 1989–1990 Bulk wt %[c]	68–76% of Bulk Glass wt %[d]	Spurr 18 Aug. 1992 Bulk wt %[e]	57–78% of Bulk Glass wt %[f]	Spurr 17–18 Sept. 1992 Bulk wt %[e]	57–78% of Bulk Glass wt %[f]
SiO_2	64.1	71.5	60.2	77.7	56.7	62.3	57.9	63.0
TiO_2	0.65	0.37	0.56	0.32	0.69	0.59	0.69	0.53
Al_2O_3	18.0	15.0	18.4	12.0	19.0	16.5	19.1	16.6
FeO*	4.1	2.3	5.8	1.24	7.1	5.6	5.9	5.1
MgO	2.0	0.5	2.3	0.20	3.7	2.0	3.7	1.9
CaO	4.8	2.3	6.8	0.9	7.6	5.4	7.4	5.2
Na_2O	4.7	4.7	4.1	3.7	3.9	5.3	4.0	5.3
K_2O	1.45	2.0	1.5	3.8	0.88	1.39	0.97	1.43
Total	99.80	98.67	99.66	99.86	99.57	99.08	99.66	99.06

[a]The glass proportions and other mineral components are also listed, along with sources of additional chemical data.

[b]*Rose et al.* [1983, Table 4, p. 143]. In addition to an average of 64 wt % glass, the ash contains, in decreasing proportions, plagioclase feldspar, opx, amphibole, magnetite, ilmenite, and cpx.

[c]*Nye et al.* [1994, Table 4, p. 442]. In addition to 68–76 wt % glass, the ash contains in decreasing proportions, plagioclase feldspar ($An_{39–88}$), hornblende, cps, opx, magnetite, and ilmenite.

[d]*Swanson et al.* [1994, Table 4, p. 458] (sample 90AMM5).

[e]*Nye et al.* [1995, Table 2, p. 123] (sample 9209268 (August) and sample Stop35 (September)). In addition to 57–78 wt % glass, the ash contains, in decreasing proportions, plagioclase feldspar (August, $An_{22–84}$; September, $An_{27–64}$), opx, magnetite, amphibole, and cpx.

[f]*Swanson et al.* [1995] (their Table 2, p. 133 (August), and Table 3, p. 134 (September)).

the samples might be enriched because of atmospheric fractionation processes [see *Rose and Chesner*, 1987] that occur because the mineral phases do not fragment to fine particles and therefore they fall out of the atmosphere more quickly and are therefore underrepresented in distal ashfalls.

3.1.1. Mount St. Helens, Washington

[10] Mount St. Helens Volcano is located in southwest Washington, United States (46.20°N, 122.18°W). Its eruption of 18 May 1980 [*Lipman and Mullineaux*, 1981] produced a volcanic cloud that circled the Earth and an ashfall deposit that extended from the volcano hundreds of kilometers to the east [*Sarna-Wojcicki et al.*, 1981]. The eruption lasted ~9 hours, and there were extensive deposits of pyroclastic flows that accumulated on the north side of the volcano. We sampled these pyroclastic flow deposits at a point 6 km north of the crater ("pumice pond" in Plate 1 of *Lipman and Mullineaux* [1981]). This sample retained much of its fine fraction because it was not subject to atmospheric fractionation like many fall materials. In fact, we screened the sample to remove the coarse fraction (>2 mm) completely. In addition, for the light-scattering measurements, the particles were sieved to remove the largest particles (see section 3.3).

3.1.2. Redoubt Volcano, Alaska

[11] Redoubt Volcano, Cook Inlet, Alaska (60.5°N, 152.7°W), is 283 km southwest of Anchorage. The Redoubt eruption of 1989–1990 lasted from 14 December until 31 August and consisted of ash eruptions and dome extrusions accompanied by block and ash flows that had ash clouds associated with them [*Brandtley*, 1990]. We studied two ash samples collected in February 1990, from ashfalls of the earlier part of Redoubt's eruptive sequence. A description of the context of these samples is given by *Scott and McGimsey* [1994]. Both of these samples originated from gas elutriation of a pyroclastic flow, a process that creates a fine ash [*Scott and McGimsey*, 1994]. Although these samples were collected at sites 10 km and 200 km from the volcano, both are quite fine grained, enriched in elutriated fines.

3.1.3. Crater Peak, Mount Spurr Volcano, Alaska

[12] Crater Peak is a smaller cone and crater on the south side of Mount Spurr, across Cook Inlet, 125 km west of Anchorage, Alaska (61.39°N, 152.25°W). In 1992, Mount Spurr had three subplinian eruptions, each reaching stratospheric heights and each lasting only a few hours [*Rose et al.*, 2001]. We studied four samples from Spurr's 1992 eruptions, two each from the 18 August and 17–18 September 1992 eruptions. The 18 August samples (sample 47) fell at Anchorage, 130 km east of the volcano and 270 km southeast (sample 43) (a map of the fallout pattern of ashes with the numbers of the collected ashes located is given by *McGimsey et al.* [2001], and a discussion of the eruption and fallout emphasizing the fine particles is given by *Rose et al.* [2001] (see especially their Figure 7b)). The 17–18 September samples fell 185 km east of the volcano (sample 33) and 265 km east of the volcano (sample 46) (a map of the fallout pattern of ashes with the numbers and collected ashes located is given by *McGimsey et al.* [2001], and a discussion of the eruption and fallout emphasizing the fine particles is given by *Rose et al.* [2001] (see especially their Figure 7c). Additional

study of the nature of Spurr ashfall is reported by *Riley et al.* [2003].

3.2. Shape Analysis

[13] Volcanic ashes present a wide variety of irregular shapes. According to *Riley et al.* [2003], volcanic ash particles can be categorized as vesicular, nonvesicular, and miscellaneous. In Figure 1 we present some scanning electronic microscope (SEM) pictures of the volcanic ashes studied in this work. It should be noted that the SEM pictures are not necessarily representative of the size distribution (for that purpose, we refer the reader to Figure 3). As shown in Figure 1, the Mount St. Helens, Redoubt, and Mount Spurr samples contain vesicular particles (Figures 1a, 1c, 1e, and 1h) and crystals with sharp edges (Figures 1b and 1d). Some vesicular particles of the Mount Spurr samples also contain small crystals (circled particles in Figure 1g).

[14] We have done a simplistic shape analysis of three of the volcanic ash samples studied in this work, i.e., Mount St. Helens, Spurr Anchorage, and Spurr 33 Stop. For that purpose, we have analyzed SEM pictures taken from particles that are distributed over carbon tape that was held briefly in the particle jet of our aerosol generator. A total of 610 particles of Mount St. Helens, 1901 particles of Spurr Anchorage, and 2169 particles of Spurr 33 Stop have been studied. In this preliminary approach we characterize the shape of the particles via their two-dimensional (2-D) projections. The particle projections identified on the SEM pictures were approximated by ellipses using a standard image processing routine. A fitted ellipse has the same area as the projected shape and the same moment of inertia. We then determined the axis ratios (major/minor) of the fitted ellipses. The distribution of axis ratios is a measure of the deviation from the spherical shape. The finer structure on the surface of the particles was not taken into account. SEM pictures of the same particle taken under various viewing angles showed no indication of any preferential orientation of the particles on the carbon tape. The SEM pictures were taken with a number of different magnifications between 100 and 4000. We have not used higher magnifications since in that case the SEM images would show a background structure that impedes the identification of particles with the image-processing routines used. With this limitation, the smallest particles that can be analyzed have radii around 0.2 μm.

[15] In Figure 2 we present the histograms of the normalized number distribution of the axis ratio N (as a percentage) for Mount St. Helens, Spurr Anchorage, and Spurr 33 Stop. According to this analysis, 90% of the particles of each sample show moderate axis ratios smaller than 3. In addition, the Spurr Anchorage and Spurr 33 Stop samples (corresponding to the two different eruptions studied in this work) present very similar axis ratio distributions with mean axis ratios of 1.7 and 1.6, respectively. The Mount St. Helens sample shows a slightly larger mean axis ratio (1.9). We note that a study of a different but very similar sample of Spurr fallout by *Riley et al.* [2003, Table 2] found an axis ratio of 1.5, nearly identical to our results.

3.3. Particle Sizes

[16] The normalized projected-surface-area distributions $S(\log r)$ of our ash samples have been measured by using
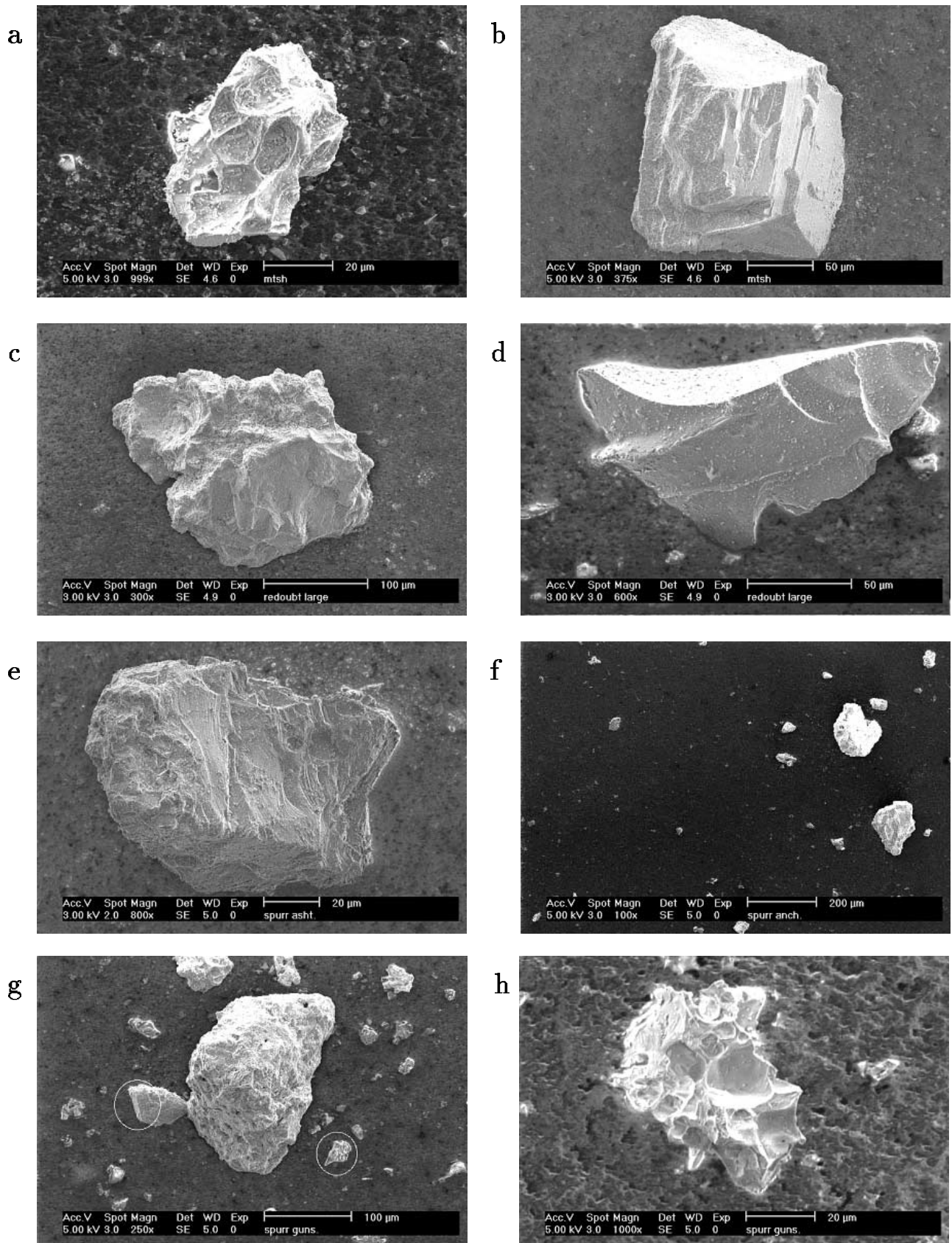
Figure 1. Examples of SEM photographs of the volcanic ashes studied: (a and b) Mount St. Helens, (c and d) Redoubt A, (e) Spurr Ashton, (f) Spurr Anchorage, and (g and h) Spurr Gunsight. In Figure 1g we have circled the vesicular particles ccontaining small crystals of the Mount Spurr sample. The white bars denote the scale of the pictures.
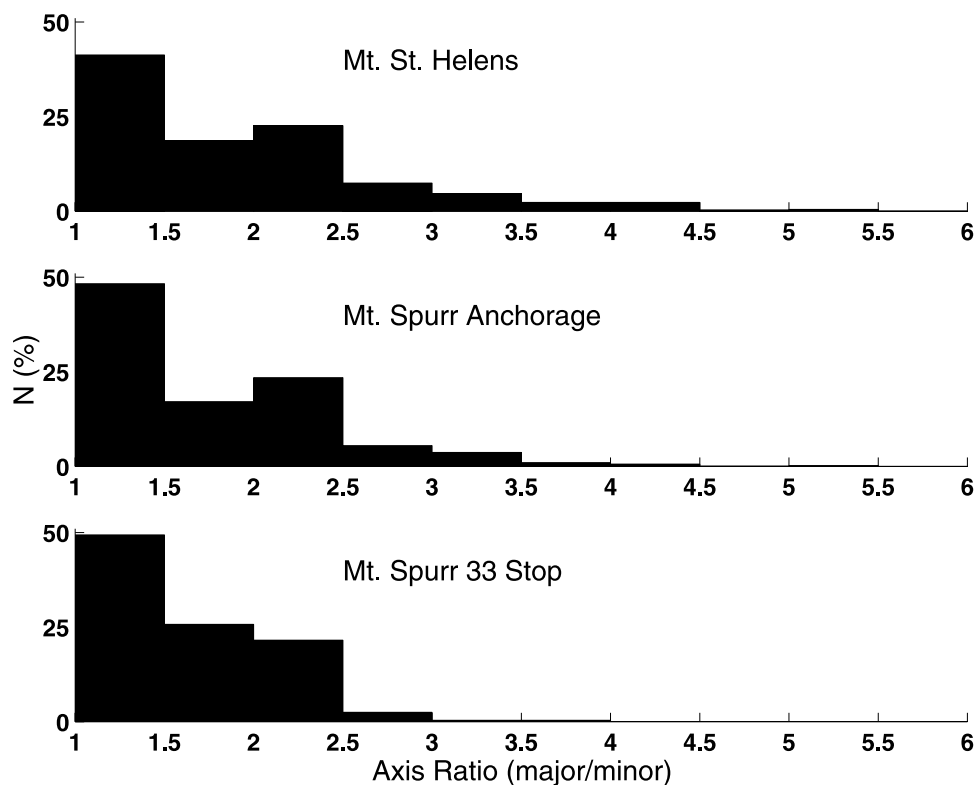
Figure 2. Histogram of the number distribution of aspect ratios in terms of the major/minor axis of fitted ellipses.

a laser particle sizer that is based on diffraction without making assumptions about the refractive indices of the materials of the particles [*Konert and Vandenberghe*, 1997]. The equivalent-sphere radius r of a nonspherical particle is defined as the radius of a sphere that has a projected area equal to the projected area of the non-spherical particle averaged over all orientations. We used a sieve with a grid width of 200 μm to sieve the Mount St. Helens, Redoubt A, and Redoubt B samples to remove the millimeter-sized particles, which are too large to be handled by the rotating brush of our aerosol generator. Figure 3 (top left panel) shows the normalized projected-surface-area distributions $S(\log r)$ as a function of r in micrometers on a logarithmic scale for the Mount St. Helens, Redoubt A, and Redoubt B before and after sieving. In that plot we can see that the size distributions have not been severely changed after the sieving. In the top right panel we show $S(\log r)$ as a function of r for the seven volcanic ash samples with the final size distributions used in the light-scattering experiment. In those plots, $S(\log r)d(\log r)$ is the relative contribution of projected-surface-equivalent spheres with radii in the size range from $\log r$ to $\log r + d(\log r)$ to the total projected area of all particles per unit volume. In Figure 3 (bottom left and right panels) the corresponding normalized number distributions $N(\log r)$ are presented, since these are often used in calculations and reported in the literature. Here $N(\log r)d(\log r)$ is the relative number of equivalent spheres with radii in the interval $d(\log r)$. These distributions were not measured, but deduced from $S(\log r)$, and should therefore be treated with more caution.

[17] Values of the effective radius r_{eff} and effective variance v_{eff} of each sample are given in Table 1. These two parameters are defined as follows:

$$r_{\mathrm{eff}} = \frac{\int_0^\infty r\pi r^2 n(r)dr}{\int_0^\infty \pi r^2 n(r)dr}, \tag{2}$$

$$v_{\mathrm{eff}} = \frac{\int_0^\infty (r - r_{\mathrm{eff}})^2 \pi r^2 n(r)dr}{r_{\mathrm{eff}}^2 \int_0^\infty \pi r^2 n(r)dr}, \tag{3}$$

where $n(r)dr$ is the fraction of the total number of projected-surface-equivalent spheres with radii in the size range $[r, r + dr]$ per unit volume of space [*Hansen and Travis*, 1974]. Here, $n(r)$ is also computed from $S(\log r)$, and we have $n(r) = N(\log r)/r \ln 10$, where $\ln$ stands for the natural logarithm. As shown in Figure 3, the seven ash samples seem to be similar in size.

[18] As mentioned in section 2, in our experiment the ensemble of ash particles under study is located in a jet stream produced by an aerosol generator where a piston pushes the powder onto a rotating brush at a certain speed. Usually, the brush removes the powder uniformly from across the whole exposed surface of the compacted powder. However, according to the specifications of our aerosol generator, particles larger than 100 μm do not pass through the brush at the same efficiency as do smaller particles. As
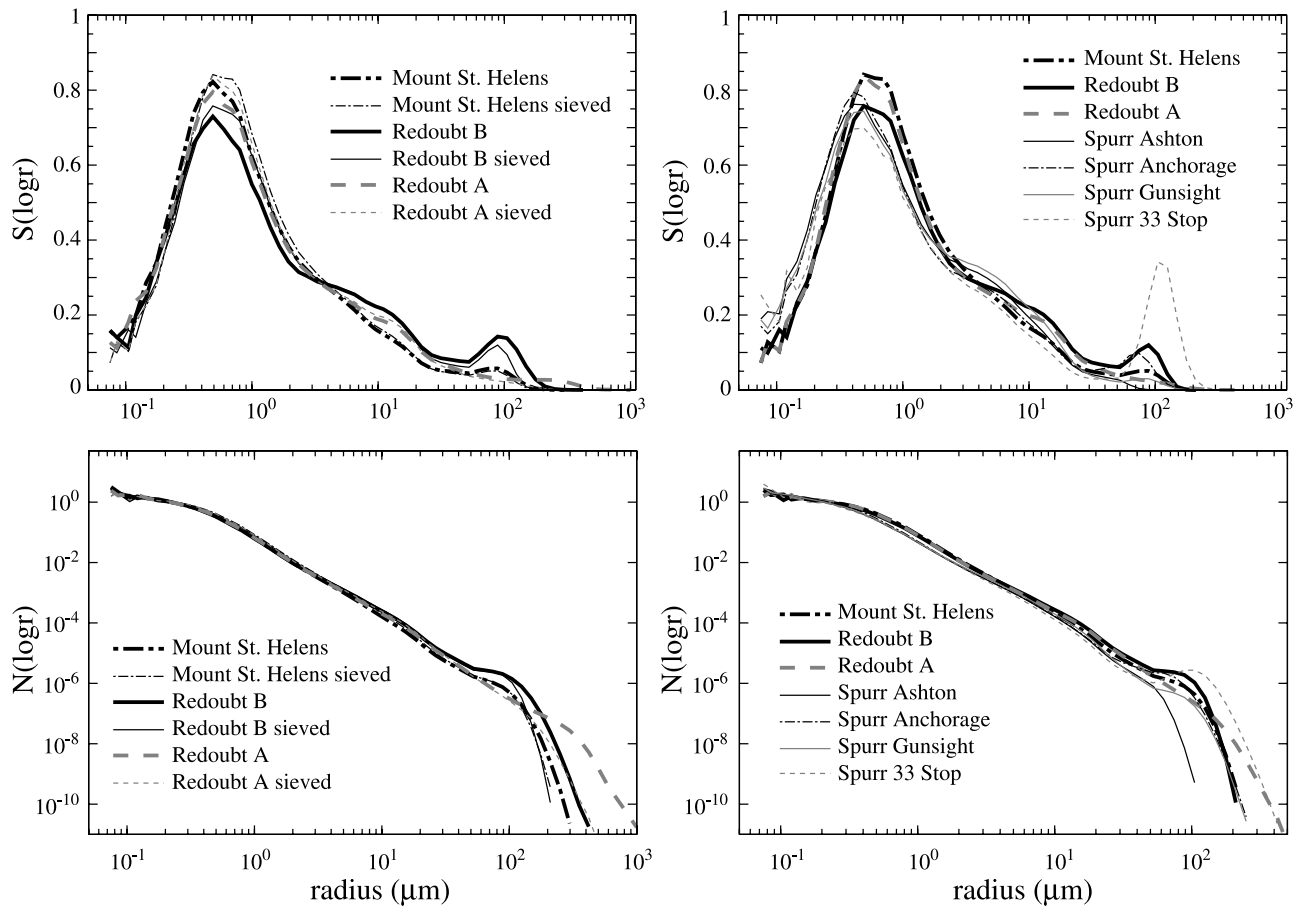
Figure 3. (top) Measured projected normalized surface area distributions and (bottom) corresponding normalized number distributions. The distributions are plotted as functions of the radius in micrometers on a logarithmic scale.

shown in Figure 3, the seven samples studied in this work have a small percentage of particles larger than 100 μm in radius (even after sieving). Therefore we have checked the percentage of particles larger than 100 μm that are not carried off by the brush into the particle jet. The volume of large particles (larger than 100 μm in radius) left in the reservoir is between 1% and 2% depending on the sample. These differences in the size distribution of the samples as they are measured in the light-scattering experiment compared with the size distributions measured with the diffraction technique led to an error in the worst case of less than 2%.

[19] *Riley et al.* [2003, Figure 5b] report a size distribution for an ash very similar to the other Spurr ashes studied here, but plotted as mass proportions. This plot demonstrates that the larger particles, though few in number, are important on a mass basis and that particles ranging from 10 to 100 μm make up the bulk of the mass.

3.4. Refractive Indices

[20] Silicate glass with composition between 57 and 78% SiO_2 has a real part of the refractive index n at visible wavelengths that varies inversely from 1.56 at 57% SiO_2 to 1.48 at 77% SiO_2 [*Williams et al.*, 1982, Figures 2−11, p. 73]. *Patterson* [1981] did absorption measurements on ashes from the 18 May 1980 Mount St. Helens eruption

collected at different surface locations. The samples were separated into two groups: One group was characterized by the pale gray color of the ash, and the other was characterized by a darker gray appearance. These ash colors corresponded to two major pulses of ash ejection by the volcano. The first dust pulse was reported to be darker, changing the color of the ash of the second pulse to pale gray. *Patterson* [1981] obtained values for the imaginary part of the refractive index k for the darker gray samples and the pale gray samples. The measured values of k at red wavelengths varied from ~0.0018 for the pale gray samples to 0.004 for the darker gray samples. Our Mount St. Helens sample from the 18 May 1980 eruption was collected from the afternoon part of the eruption and was a pyroclastic flow; its imaginary part of the refractive index is more likely to be similar to Patterson's pale gray sample ($k \sim 0.0018$).

[21] For the other volcanic ash samples no measured refractive indices in the visible are available in the literature. *Winchester* [1998] experimentally determined the complex refractive indices of ashes of Mount St. Helens and Mount Spurr in the ultraviolet (eight different wavelengths between 309 and 380 nm). He found the real part of the refractive index to vary between 1.74 at 309 nm and 1.62 at 380 nm for Mount St. Helens ash and between 1.51 at 309 nm and 1.57 at 369 nm for Mount Spurr ash and the imaginary part of the refractive index to depend little on wavelength for
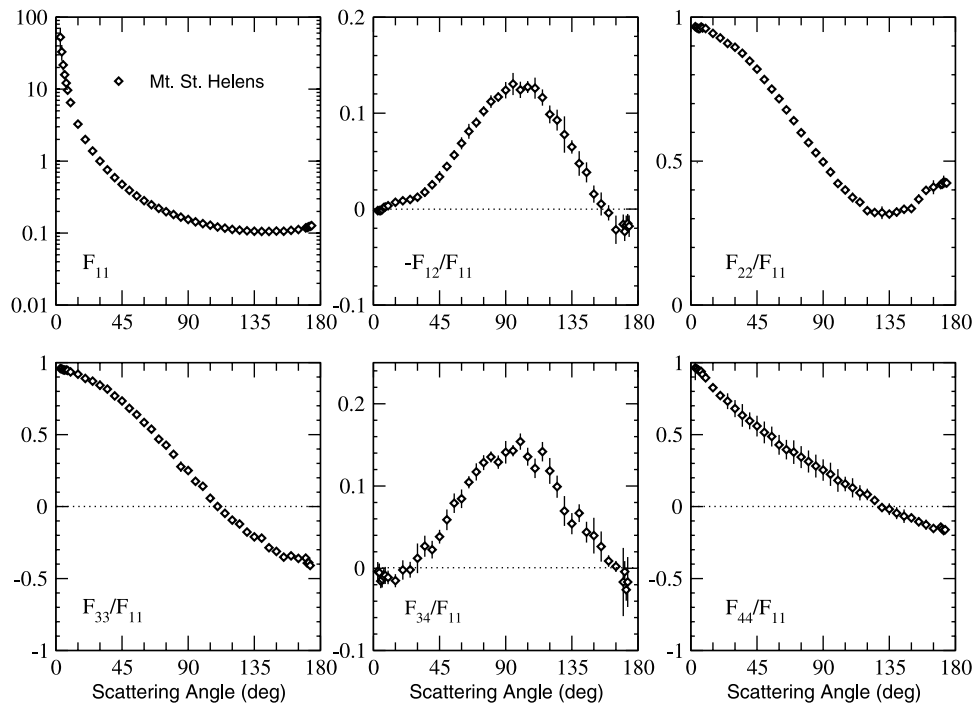
Figure 4. Measured scattering matrix elements as functions of the scattering angle at 632.8 nm for the Mount St. Helens sample. Error is indicated by bars or is within the size of the symbols.

both samples, with values between 2.0×10^{-3} and 3.1×10^{-3} for Mount St. Helens ash and between 4.8×10^{-3} and 6.0×10^{-3} for Mount Spurr ash. Since there is little difference between the colors of the Mount St. Helens ash and the Redoubt ash, we assume that the imaginary parts of their refractive indices in the red part of the spectrum are also very similar. In contrast, Mount Spurr ash shows a darker gray color than does the Mount St. Helens sample. *Patterson* [1981] reports measurements of the imaginary part of the refractive index for Fuego ash, which exhibits a dark gray color. He gives a value of the imaginary part of the refractive index for Volcan de Fuego ash of ~0.02 at 650 nm. Thus our Mount Spurr ash samples are expected to have a value of the imaginary part of the refractive index between 0.0018 and 0.02.

4. Measurements

[22] In Figures 4, 5, and 6 we present the experimentally determined scattering matrix elements at 632.8 nm as functions of the scattering angle θ in the range $3°-174°$ for Mount St. Helens, Redoubt, and Mount Spurr ash samples, respectively. All scattering functions or phase functions $F_{11}(\theta)$ are shown on a logarithmic scale and normalized to 1 at $\theta = 30°$. Hence the scattering functions are measured on a relative scale, and these do not depend on the number of particles. The other elements of the matrix are normalized to F_{11}; that is, we consider $F_{i,j}/F_{11}$, with $i, j = 1-4$ with the exception of $i = j = 1$. The experimental errors are indicated by error bars. When no error bar is shown, the value for the standard deviation of the mean value is smaller than the symbol plotted. The elements $F_{13}(\theta)/F_{11}(\theta)$, $F_{14}(\theta)/F_{11}(\theta)$, $F_{23}(\theta)/F_{11}(\theta)$, and $F_{24}(\theta)/F_{11}(\theta)$, were found to be zero over their entire angle range within the accuracy of the

measurements. As mentioned in section 2, this implies that we have to consider only six elements of the 4×4 scattering matrix. Consequently, we will interpret $-F_{12}(\theta)/F_{11}(\theta)$ as the degree of linear polarization for unpolarized incident light.

[23] As shown in these figures, in general, the scattering matrix elements for the seven volcanic ash samples follow the general trends presented by irregular mineral particles [*Mishchenko et al.*, 2000; *Volten et al.*, 2001] and show relatively little differences. Nevertheless, we will attempt to discuss and interpret these differences. As discussed in section 3.2, the shapes of the particles of the seven volcanic ash samples are quite similar to each other and in any case not important enough to produce differences in the scattering patterns. Therefore the differences in the scattering behavior of our samples might be produced by the small differences in the size and color of our samples. In all cases the measured $F_{11}(\theta)$ are flat functions of the scattering angle with a strong forward peak and almost no structure at side-scattering and backscattering angles. The steepness of the $F_{11}(\theta)$ curves, defined as the measured maximum value of $F_{11}(\theta)$ divided by the measured minimum value over the scattering angle range $3°-174°$, varies from ~500 for the Mount St. Helens ash sample to 400 for the Redoubt A ash sample (see Figure 7). The steepness of $F_{11}(\theta)$ depends on the size and complex refractive index of the particles [*Volten et al.*, 2001]. Since the seven volcanic ash samples studied in this work present very similar effective size parameters, it is not surprising that we do not find clear trends in the steepnesses in relation to the size of the particles. *Volten et al.* [2001] found a trend that dark-colored samples show larger steepnesses than light-colored samples. In our case, all samples present relatively light colors (different scales of gray). By comparing samples corresponding to the same volcanic
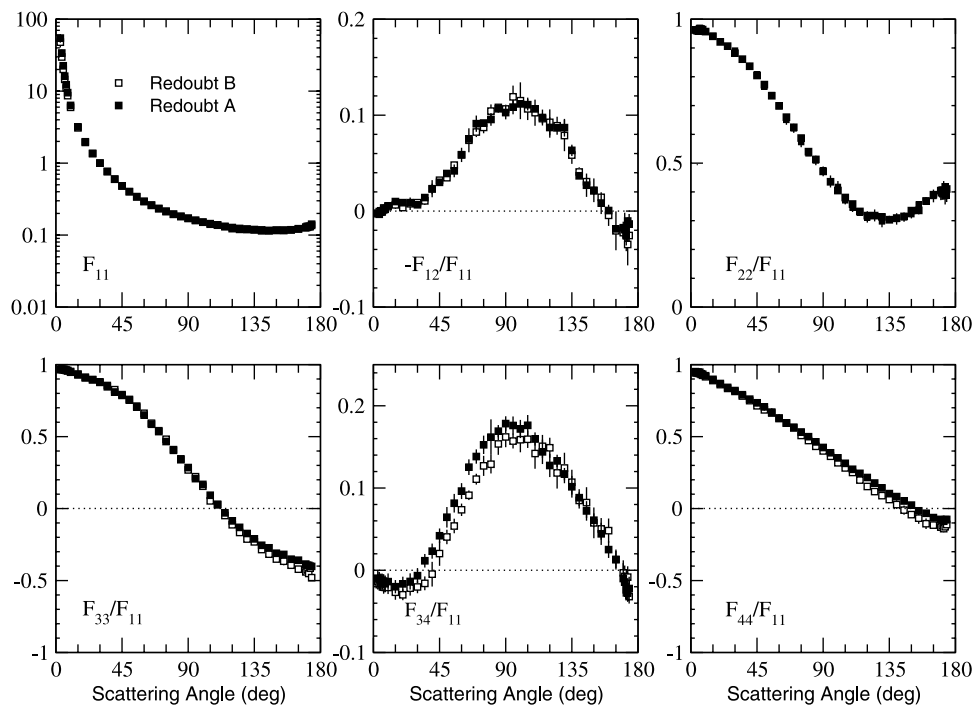
Figure 5. As in Figure 4, but for the Redoubt A and B samples.

eruption that are very similar in composition (see Table 2) and therefore in color, we generally find a larger steepness for the samples with larger effective radius. The steepness of Spurr Anchorage (r_{eff} = 4.8 μm and v_{eff} = 8.8), for example, is larger than the steepness of Spurr Ashton (r_{eff} = 2.7 μm and v_{eff} = 4.9). Furthermore, the $F_{11}(\theta)$ curve for Spurr 33 Stop (r_{eff} = 14.4 μm and v_{eff} = 6.6) is steeper than the $F_{11}(\theta)$

curve for Spurr Gunsight (r_{eff} = 3.5 μm and v_{eff} = 8.2). In contrast, we find the opposite effect for Redoubt A (r_{eff} = 4.1 μm and v_{eff} = 9.7) and Redoubt B (r_{eff} = 6.4 μm and v_{eff} = 7.6). Here the steeper $F_{11}(\theta)$ curve corresponds to Redoubt A, which is the sample with the smallest effective radius. When we look at v_{eff}, we see that the largest steepness is found in two cases for the largest v_{eff} (Redoubt A and Spurr
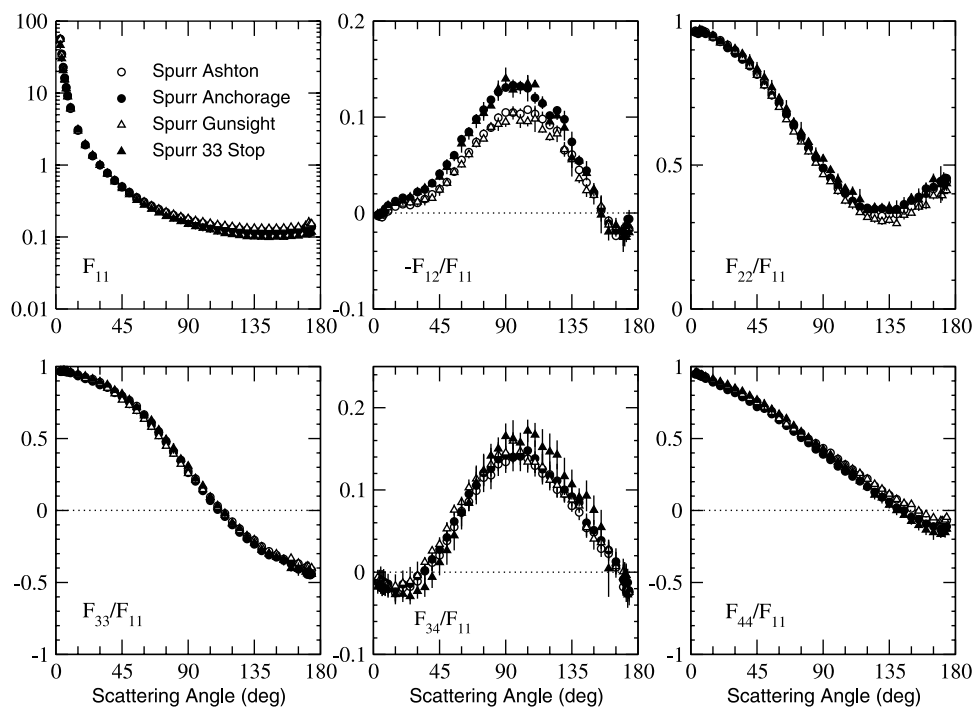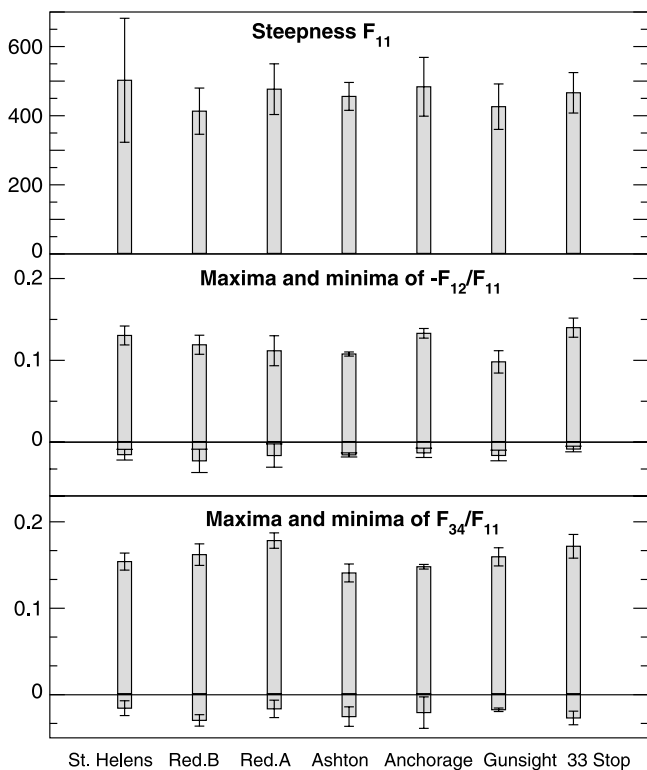

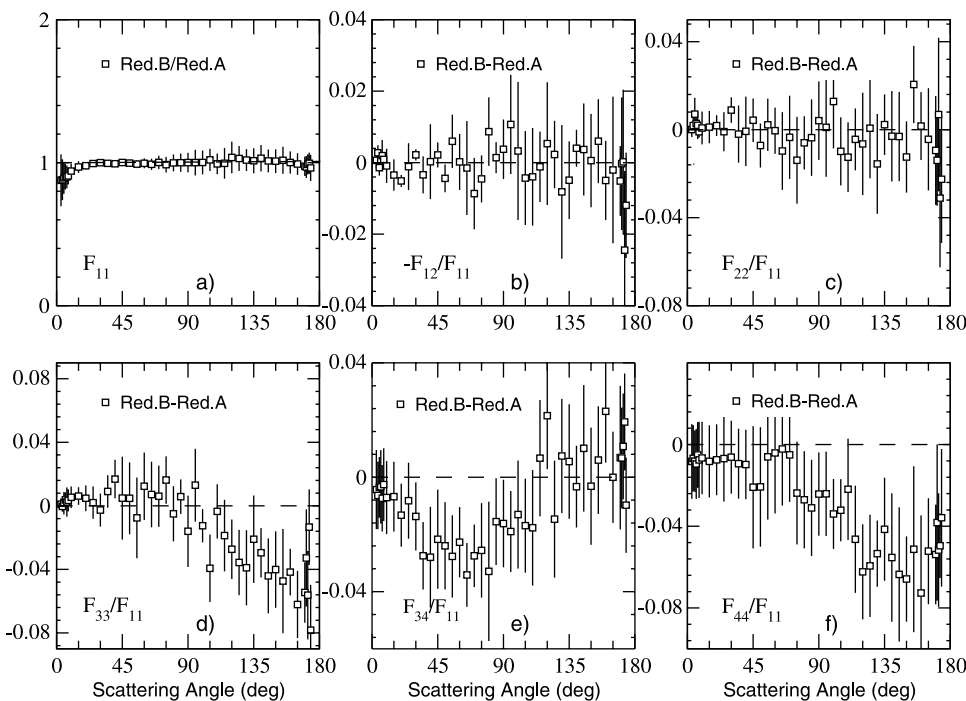**Figure 6.** As in Figure 4, but for the samples Spurr Ashton, Spurr Anchorage, Spurr Gunsight, and Spurr 33 Stop.

Figure 7. Properties of the measured scattering matrix elements. (top) Steepnesses of $F_{11}(\theta)$. (center) Maximum and minimum measured values of $-F_{12}(\theta)/F_{11}(\theta)$. (bottom) Maximum and minimum measured values of $F_{34}(\theta)/F_{11}(\theta)$. Error bars are also shown.

Anchorage). However, we find the opposite trend for Spurr Gunsight. Therefore the steepness may be determined by the width of the size distribution as well.

[24] In Figures 8a and 9a we present the ratios of the measured values of $F_{11}(\theta)$ for the samples collected from the same volcanic eruption. In Figure 8 we observe only a slightly steeper forward scattering peak for Redoubt A, the sample with a smaller r_{eff} but a slightly larger v_{eff}. We find the same trend for Spurr Gunsight and Spurr 33 Stop. The sample with a steeper forward scattering peak (Spurr Gunsight) shows a considerably smaller r_{eff} but a slightly larger v_{eff}. For the Spurr Ashton and Anchorage samples we find the same trend in relation to r_{eff}; that is, the sample with the slightly steeper forward scattering peak (Spurr Ashton) presents the smallest r_{eff} and also the smallest v_{eff} (see Table 1).

[25] As already mentioned, the ratio $-F_{12}(\theta)/F_{11}(\theta)$ represents the degree of linear polarization for incident unpolarized light. Also for this ratio we see in Figures 4–6 that all measured ratios present similar shapes, but we observe some differences in their maxima and minima. As shown in Figure 7 the highest maxima of the degree of linear polarization are presented for the Mount St. Helens sample and the Spurr Anchorage sample, which have a larger v_{eff}, so that also here v_{eff} may play a subtle role in the scattering behavior. In contrast, the Spurr 33 Stop sample, which also shows a higher maximum of $-F_{12}(\theta)/F_{11}(\theta)$ as compared with Spurr Gunsight sample, has the smallest v_{eff} and a remarkably larger r_{eff}. All measured $-F_{12}(\theta)/F_{11}(\theta)$ curves lie below zero beyond around 160°. When comparing the results for samples collected from the same volcanic eruption (Figures 8 and 9), we see that the maximum of $-F_{12}(\theta)/F_{11}(\theta)$

Figure 8. (a) Measured $F_{11}(\theta)$ for Redoubt B divided by the measured $F_{11}(\theta)$ for Redoubt A. (b–f) Differences between the indicated measured ratios for Redoubt B and Redoubt A.
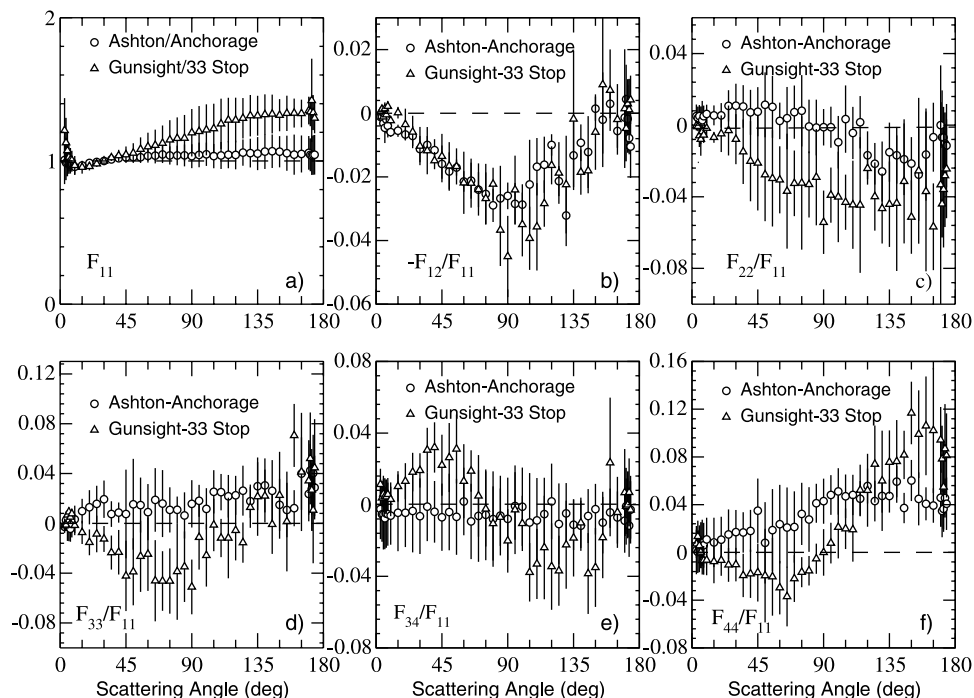
Figure 9. As in Figure 8, but for the Spurr Ashton and Anchorage samples (circles) as well as the Spurr Gunsight and 33 Stop samples (triangles).

presents larger differences for the Mount Spurr samples than for the Redoubt samples.

[26] The measured values of $F_{22}(\theta)/F_{11}(\theta)$ prove that the scattering behavior of our ash samples is different from that of homogeneous optically inactive spheres since, for such spheres, $F_{22}(\theta) \equiv F_{11}(\theta)$. The $F_{22}(\theta)/F_{11}(\theta)$ curves decrease from close to 1 at forward directions to ∼0.3 around 135°, increasing again to ∼0.4 at backward directions. *Volten et al.* [2001] found that for irregular particles this ratio is also affected by the size of the particles and their refractive indices, with the largest particles showing the deepest minima. It seems as though the differences in size, shape, and color of the particles of our samples are not significant enough to produce strong differences in the scattering behavior since we do not see strong differences between the scattering matrices of our ash samples.

[27] As shown in Figures 4–6, the $F_{34}(\theta)/F_{11}(\theta)$ ratios present the typical shapes for irregularly shaped mineral particles, with a negative minimum at small scattering angles, increasing at side-scattering angles and decreasing again at backward scattering angles [*Mishchenko et al.*, 2000; *Volten et al.*, 2001]. In Figure 8e we present the differences for the two Redoubt samples. The Redoubt A sample shows the highest values at almost all scattering angles, with the strongest differences between about 45° and 90°. In Figure 9 the Spurr Gunsight results compared to the Spurr 33 Stop sample show higher values from almost forward directions to around 90°, becoming smaller from that point on to almost backward directions. However, the $F_{34}(\theta)/F_{11}(\theta)$ curves present the same values (within the error bars) for the Spurr Ashton and Spurr Anchorage samples.

[28] Another indication of the nonsphericity of the particles is provided by the $F_{33}(\theta)/F_{11}(\theta)$ and $F_{44}(\theta)/F_{11}(\theta)$ ratios. For homogeneous optically inactive spheres, $F_{33}(\theta)$

$\equiv F_{44}(\theta)$. However, for our volcanic ash samples this is not the case, and $F_{33}(\theta)/F_{11}(\theta)$ is zero at a smaller scattering angle than $F_{44}(\theta)/F_{11}(\theta)$ is. In addition, $F_{33}(\theta)/F_{11}(\theta)$ presents in all cases a lower minimum than $F_{44}(\theta)/F_{11}(\theta)$ does. The strongest differences in $F_{33}(\theta)/F_{11}(\theta)$ and $F_{44}(\theta)/F_{11}(\theta)$ for the two Redoubt samples are presented at large scattering angles. In that region the measured values are larger for the Redoubt A sample (see Figure 8). The measured $F_{33}(\theta)/F_{11}(\theta)$ ratios for the Spurr Ashton and Anchorage samples are very similar to each other at all scattering angles, whereas the $F_{44}(\theta)/F_{11}(\theta)$ curve for Spurr Ashton lies above the measured curve for the Spurr Anchorage sample at angles larger than around 45°. In contrast, the values of $F_{33}(\theta)/F_{11}(\theta)$ for the Spurr 33 Stop sample are generally larger than those obtained for the Spurr Gunsight sample except for angles larger than 140°, where the values for the Spurr Gunsight sample become larger than the values for the Spurr 33 Stop sample. We observe the same tendency for $F_{44}(\theta)/F_{11}(\theta)$, although in this case the values for the Spurr Ashton sample become larger than the values for the Spurr Anchorage sample at smaller scattering angles (∼90°).

4.1. Lorenz-Mie Calculations Versus Measured Scattering Matrix

[29] In Figure 10 we compare the measured scattering matrix elements as functions of the scattering angle for the Mount St. Helens sample with results of Lorenz-Mie calculations [*Mie*, 1908] for homogeneous optically non-active spherical particles. We have chosen this sample for the comparison since we know its refractive index with a higher accuracy than for the other samples (see section 3.4). For the Lorenz-Mie calculations we employed the relative number size distribution $n(r)$ derived from the measured projected-surface-area distribution for the Mount St. Helens
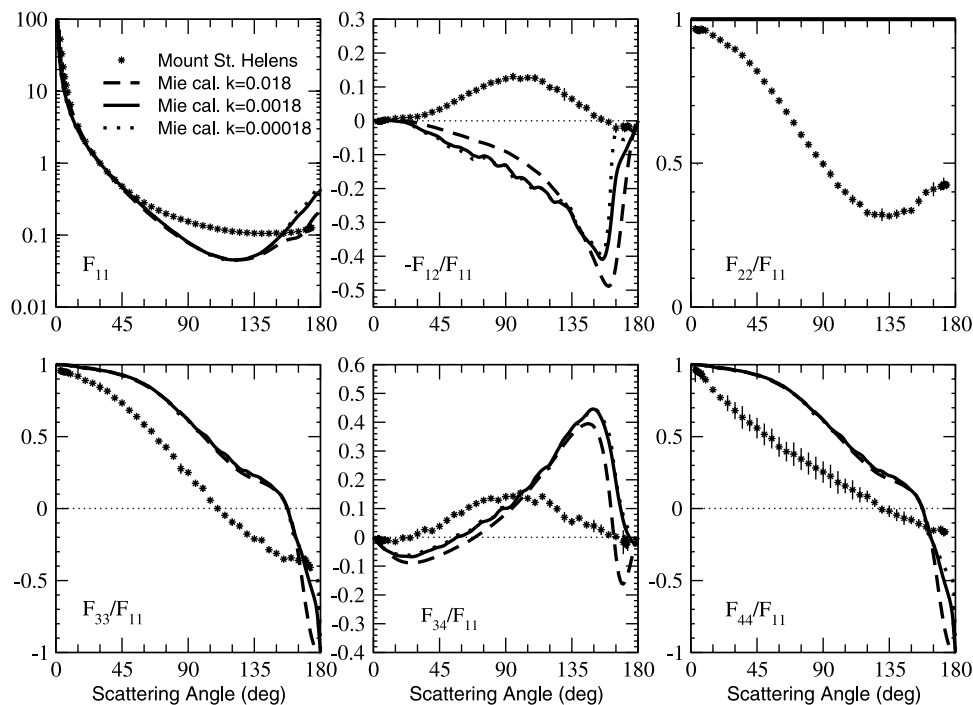
Figure 10. Measured scattering matrix elements as functions of the scattering angle at 632.8 nm for the Mount St. Helens sample. The measurements are presented together with results of Lorenz-Mie calculations for spheres with the same size distribution as the Mount St. Helens sample. For the calculations the real part of the refractive index was fixed at 1.5, and the imaginary part was varied between 0.018 (dashed lines), 0.0018 (solid lines), and 0.00018 (dotted lines).

sample shown in Figure 3. The imaginary part of the refractive index k was fixed at $k = 0.0018$ (solid lines) according to the value given by *Patterson* [1981]. In order to check the effect of a higher or lower value of k we also present calculations for $k = 0.018$ (dashed lines) and $k = 0.00018$ (dotted lines). The real part of the refractive index was fixed at 1.5 (see section 3.4). The calculated phase function has also been normalized to 1 at 30°. As shown for that element in Figure 10, the relative differences between the calculated and experimental scattering functions are quite strong at side-scattering and backscattering angles. Significant differences between measured and calculated values are also found for the other scattering matrix elements. In particular, the measured degree of linear polarization for incident unpolarized light $-F_{12}(\theta)/F_{11}(\theta)$ is positive at almost all scattering angles whereas the calculated values tend to be negative at almost all scattering angles. $F_{22}(\theta)/F_{11}(\theta)$ is equal to 1 at all scattering angles for spherical particles while the measured results for our Mount St. Helens ash sample strongly deviate from 1 with a minimum of 0.32 near 135°. Similarly, $F_{44}(\theta)/F_{11}(\theta)$ tends to be larger than $F_{33}(\theta)/F_{11}(\theta)$ whereas for homogeneous optically nonactive spheres these are equal at all scattering angles. In addition, the calculated values of $F_{34}(\theta)/F_{11}(\theta)$ are smaller than the measured ones up to ∼90°, after which the reverse is true for most angles.

4.2. Average and Synthetic Scattering Matrix for Volcanic Ashes

[30] From the comparison of the measured scattering matrix elements for the Mount St. Helens sample with

results of Lorenz-Mie calculations presented in section 4.1 we can see that Mie calculations should not be used to describe the scattering behavior of irregular volcanic ash particles. As an alternative we create an average scattering matrix for volcanic ashes. The motivation for this is the high similarity in the scattering behavior of the distinct volcanic ash samples presented in this work and those previously published by *Volten et al.* [2001] and *Muñoz et al.* [2002]. Therefore, although detailed differences are present in the measured scattering matrices, we consider it justified to construct an average volcanic ash scattering matrix for use, for example, in studies of climatic effects of a volcanic eruption when the actual properties of the volcanic ash are not known.

[31] The average volcanic ash scattering matrix was obtained as follows. First, the average volcanic ash phase function $F_{11}(\theta)$ was determined by averaging the seven measured phase functions for volcanic ash particles presented in this work and the two phase functions of Lokon, as well as the Pinatubo volcanic ash at 632.8 nm presented by *Volten et al.* [2001] and *Muñoz et al.* [2002]. Since no scattering cross sections are available, the phase functions were averaged, giving them equal weights. Thus the normalization to unity at 30° also holds for the average phase function. Second, each measured element ratio was multiplied with its corresponding normalized phase function. Third, for each pair of indices (i, j) the elements $F_{i,j}$ of the average scattering matrix were obtained by averaging the nine corresponding elements. Finally, division by the average phase function yielded the element ratios of the average aerosol scattering matrix. The resulting average
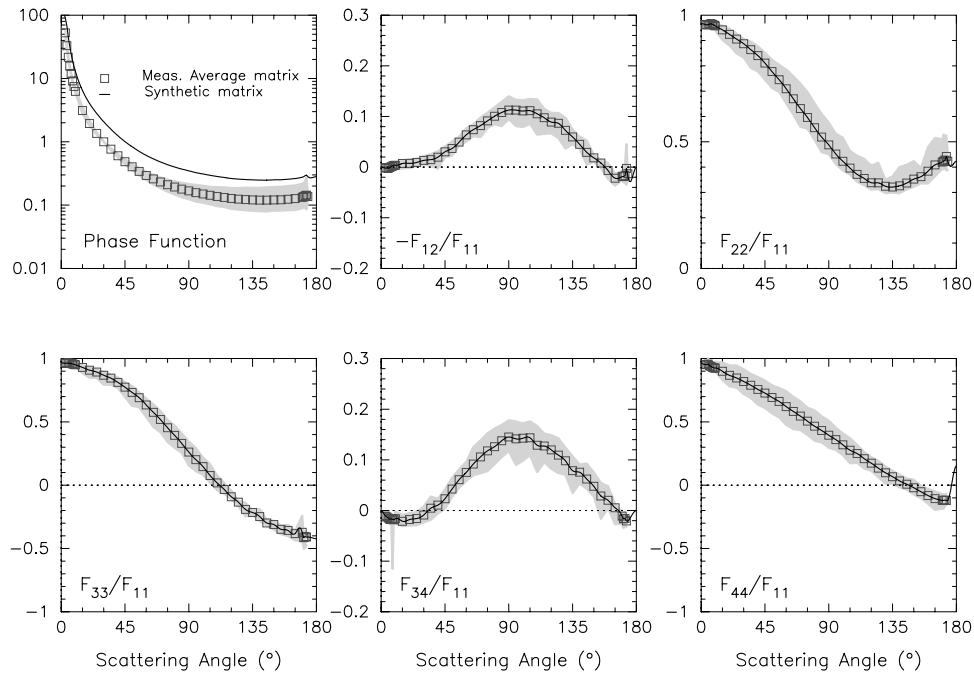
Figure 11. Average scattering matrix element $F_{11}(\theta)$ and element ratios $-F_{12}(\theta)/F_{11}(\theta)$, $F_{22}(\theta)/F_{11}(\theta)$, $F_{33}(\theta)/F_{11}(\theta)$, $F_{34}(\theta)/F_{11}(\theta)$, and $F_{44}(\theta)/F_{11}(\theta)$ (squares). The domains occupied by the measurements used to obtain the average are indicated with gray shading. Solid lines correspond to the synthetic scattering matrix elements $S_{i,j}$. Note that $F_{11}(\theta)$ (squares, top left corner) is normalized to unity at $30°$ whereas $S_{11}(\theta)$ (solid line, top left corner) is normalized so that its average over all directions equals unity.

matrix satisfies the Cloude test at each measured scattering angle.

[32] As mentioned in section 2, the experimental measurements do not cover either the exact forward scattering or the exact backward scattering direction. Therefore what we obtain is the relative phase function, $F_{11}(\theta) = S_{11}(\theta)/S_{11}(30°)$, in which $S_{11}(\theta)$ is the phase function, normalized so that its average over all directions equals unity, i.e.,

$$\frac{1}{2} \int_o^\pi d\theta \sin\theta S_{11}(\theta) = 1. \qquad (4)$$

This limits the use of the average scattering matrix data for radiative transfer calculations. To facilitate the use of the average scattering matrix for multiple-scattering calculations, we have constructed a synthetic scattering matrix based on the average scattering matrix. The synthetic scattering matrix is defined in the full range from $0°$ to $180°$. For the extension of the phase function we have followed the procedure described by *Liu et al.* [2003], which is based on the assumption that the diffraction forward scattering peak for small randomly oriented particles with moderate aspect ratios mainly depends on the size of the particles and is largely independent of their shapes and refractive indices [*Mishchenko et al.*, 1996, 1997]. Thus we have merged the measured average phase function with the results of Lorenz-Mie calculations for projected-surface-area equivalent spheres between $0°$ and $3°$. For the Lorenz-Mie calculations we have used an average size distribution and the refractive index of the Mount St. Helens sample. The precise choice of the refractive index is not relevant for the results of the Lorenz-Mie calculations at very small scattering angles

since, as mentioned, the forward scattering peak is independent of the refractive index. In any case, this has been checked by performing Lorenz-Mie calculations for different values of n and k, for which we did not find significant differences in the calculated results. The size distribution used for the calculations is a normalized number distribution of projected-surface-area-equivalent spheres obtained as follows. First we averaged the measured normalized surface distribution at each radius interval given in the laser particle sizer measurements. This procedure provided an average surface distribution as a function of r in micrometers. The average surface distribution was renormalized and transformed into a number size distribution (see, e.g., http://www.astro.uva.nl/scatter/ for detailed information on how to transform one type of size distribution into another). As outlined above, the results of the Lorenz-Mie calculations for the scattering angle interval from $0°$ to $3°$ were merged with the average phase function $F_{11}(\theta)$, which was scaled until the normalization condition (equation (4)) was satisfied. Hereby the average phase function was extrapolated to $180°$ assuming a smooth run of the function $F_{11}(\theta)$.

[33] For the relative scattering matrix elements F_{ij}/F_{11} a cubic spline extrapolation is used for both the forward scattering and backscattering directions. Values at exact forward and backward scattering were determined so that they satisfy the conditions given by *Hovenier and van der Mee* [2000]. In addition, the element ratios must run as smoothly as possible toward $0°$ and $180°$. In order to achieve this, a fit algorithm was applied that takes into account the experimental error bars in such a way that if the error is small, the measured value has a strong influence on

Table 3. Synthetic Scattering Matrix Elements $S_{i,j}$ as Functions of the Scattering Angle

Angle, deg	S_{11}	S_{22}/S_{11}	S_{33}/S_{11}	S_{44}/S_{11}	$-S_{12}/S_{11}$	S_{34}/S_{11}
0	3.93E+03[a]	9.66E−01	9.66E−01	9.61E−01	0.00E+00	0.00E+00
1	2.89E+02	9.66E−01	9.65E−01	9.59E−01	−4.53E−04	−2.22E−03
2	1.08E+02	9.65E−01	9.63E−01	9.55E−01	−1.33E−03	−6.87E−03
3	8.81E+02	9.63E−01	9.63E−01	9.51E−01	−1.92E−03	−1.09E−02
4	6.82E+01	9.61E−01	9.64E−01	9.52E−01	−1.97E−03	−1.27E−02
5	4.49E+01	9.63E−01	9.64E−01	9.57E−01	−2.23E−03	−1.50E−02
10	1.30E+01	9.58E−01	9.50E−01	9.26E−01	3.81E−03	−1.62E−02
15	6.46E+00	9.42E−01	9.30E−01	8.99E−01	7.21E−03	−2.13E−02
20	4.03E+00	9.24E−01	9.08E−01	8.67E−01	7.36E−03	−1.79E−02
25	2.80E+00	9.06E−01	8.94E−01	8.46E−01	9.25E−03	−1.59E−02
30	2.07E+00	8.88E−01	8.68E−01	8.19E−01	1.32E−02	−8.99E−03
35	1.59E+00	8.64E−01	8.45E−01	7.89E−01	1.48E−02	4.57E−03
40	1.25E+00	8.40E−01	8.11E−01	7.56E−01	1.96E−02	1.07E−02
45	1.00E+00	8.11E−01	7.74E−01	7.27E−01	3.02E−02	2.33E−02
50	8.37E−01	7.77E−01	7.32E−01	6.93E−01	3.68E−02	4.24E−02
55	7.07E−01	7.45E−01	6.91E−01	6.61E−01	4.93E−02	6.08E−02
60	6.10E−01	7.10E−01	6.34E−01	6.21E−01	6.37E−02	7.52E−02
65	5.38E−01	6.69E−01	5.75E−01	5.83E−01	7.40E−02	9.16E−02
70	4.81E−01	6.31E−01	5.19E−01	5.45E−01	8.20E−02	1.06E−01
75	4.36E−01	5.96E−01	4.54E−01	5.06E−01	9.13E−02	1.18E−01
80	4.00E−01	5.56E−01	3.94E−01	4.67E−01	1.00E−01	1.26E−01
85	3.71E−01	5.19E−01	3.30E−01	4.32E−01	1.08E−01	1.38E−01
90	3.48E−01	4.88E−01	2.61E−01	3.95E−01	1.13E−01	1.45E−01
95	3.26E−01	4.52E−01	2.01E−01	3.60E−01	1.13E−01	1.41E−01
100	3.11E−01	4.23E−01	1.47E−01	3.19E−01	1.11E−01	1.43E−01
105	2.96E−01	3.96E−01	7.63E−02	2.76E−01	1.12E−01	1.44E−01
110	2.83E−01	3.72E−01	1.79E−02	2.50E−01	1.05E−01	1.29E−01
115	2.73E−01	3.55E−01	−3.43E−02	2.09E−01	9.76E−02	1.27E−01
120	2.63E−01	3.40E−01	−9.14E−02	1.74E−01	8.89E−02	1.20E−01
125	2.58E−01	3.38E−01	−1.34E−01	1.34E−01	8.66E−02	1.09E−01
130	2.54E−01	3.24E−01	−1.92E−01	9.79E−02	7.26E−02	9.81E−02
135	2.51E−01	3.21E−01	−2.16E−01	6.70E−02	5.96E−02	7.87E−02
140	2.49E−01	3.26E−01	−2.48E−01	3.36E−02	4.51E−02	7.56E−02
145	2.48E−01	3.37E−01	−2.98E−01	7.54E−03	2.93E−02	6.21E−02
150	2.51E−01	3.53E−01	−3.11E−01	−2.02E−02	1.84E−02	4.78E−02
155	2.52E−01	3.62E−01	−3.49E−01	−5.15E−02	8.18E−03	2.87E−02
160	2.57E−01	3.84E−01	−3.58E−01	−8.17E−02	−6.72E−03	2.02E−02
165	2.63E−01	4.09E−01	−3.83E−01	−1.06E−01	−2.19E−02	5.30E−03
170	2.76E−01	4.20E−01	−3.72E−01	−1.20E−01	−1.86E−02	−1.12E−02
175	2.72E−01	4.07E−01	−4.10E−01	−9.21E−02	−2.82E−02	−1.75E−02
176	2.69E−01	4.02E−01	−4.12E−01	−3.89E−02	−2.87E−02	−1.32E−02
177	2.71E−01	4.06E−01	−4.15E−01	2.54E−02	−2.21E−02	−8.53E−03
178	2.75E−01	4.13E−01	−4.19E−01	8.77E−02	−1.25E−02	−4.29E−03
179	2.80E−01	4.20E−01	−4.22E−01	1.35E−01	−3.79E−03	−1.20E−03
180	2.83E−01	4.23E−01	−4.23E−01	1.53E−01	0.00E+00	0.00E+00

[a]Read 3.93E+03 as 3.93×10^3.

the final solution. The resulting synthetic scattering matrix for volcanic ash particles satisfies the Cloude (coherency matrix) test at all scattering angles as described by *Hovenier and van der Mee* [1996]. The resulting fits are presented in Figure 11. In Table 3 we present the values for the synthetic average scattering matrix.

5. Conclusions

[34] In this work, we present measurements of the scattering matrices as functions of the scattering angle of seven different volcanic ash samples: Mount St. Helens ash, Redoubt A, Redoubt B, Spurr Ashton, Spurr Anchorage, Spurr Gunsight, and Spurr 33 Stop. The samples were collected after the 18 May 1980 eruption of Mount St. Helens, the 1989-1990 Redoubt eruption (Redoubt A and Redoubt B), and the 18 August 1992 and 17 September eruptions of Mount Spurr (Spurr Ashton and Spurr Anchorage, and Spurr Gunsight and Spurr 33 Stop, respectively). The measured results follow the general trends presented by

irregular mineral particles. Only relatively small, though interesting, differences were found in the phase functions, normalized so that $F_{11}(30°) = 1$, and $F_{i,j}(\theta)/F_{11}(\theta)$ ratios. Therefore we have constructed an average scattering matrix for volcanic ashes that can be used for many purposes, for example, to evaluate calculated light-scattering properties of volcanic ash particles and to constrain scattering properties of volcanic ashes that are used in radiative transfer calculations and in studies of climatic effects of volcanic eruptions when the actual properties of the volcanic ash are unknown. To facilitate the use of the average scattering matrix for multiple-scattering calculations, we also present a synthetic scattering matrix based on the average scattering matrix for volcanic ashes available in the full angle range from 0° to 180°. The synthetic scattering matrix as a function of the scattering angle is presented in a table to facilitate the use of the data. The measured results for the Mount St. Helens sample are compared with results of Lorenz-Mie calculations for projected-area-equivalent spheres with the same number distribution and refractive index as the Mount the St. Helens

ash. The experimental scattering matrix is poorly represented by the Lorenz-Mie calculations, showing strong differences between measured and calculated values in all scattering matrix elements at almost all scattering angles. Thus the use of our synthetic scattering matrix will be a much more reliable input for radiative transfer calculations and retrieval purposes than Lorenz-Mie calculations for the scattering matrix elements. The measured scattering matrices as well as the synthetic scattering matrix presented in this work are available at the Amsterdam Light Scattering Database (http://www.astro.uva.nl/scatter).

References

Brandtley, S. R. (1990), The eruption of Redoubt Volcano, Alaska, December 14, 1989–August 31, 1990, *U.S. Geol. Surv. Circ.*, *1061*, 33.

Dubovik, O., B. N. Holben, T. Lapyonok, A. Sinyuk, M. I. Mishchenko, P. Yang, and I. Slutsker (2002), Non-spherical aerosol retrieval method employing light scattering by spheroids, *Geophys. Res. Lett.*, *29*(10), 1415, doi:10.1029/2001GL014506.

Hansen, J. E., and L. D. Travis (1974), Light scattering in planetary atmospheres, *Space Sci. Rev.*, *16*, 527–610.

Hovenier, J. W. (2000), Measuring scattering matrices of small particles at optical wavelengths, in *Light Scattering by Nonspherical Particles*, edited by M. I. Mishchenko, J. W. Hovenier, and L. D. Travis, pp. 355–365, Academic, San Diego, Calif.

Hovenier, J. W., and C. V. M. van der Mee (1983), Fundamental relationships relevant to the transfer of polarized light in a scattering atmosphere, *Astron. Astrophys.*, *128*, 1–16.

Hovenier, J. W., and C. V. M. van der Mee (1996), Testing scattering matrices: A compendium of recipes, *J. Quant. Spectrosc. Radiat. Transfer*, *55*, 649–661.

Hovenier, J. W., and C. V. M. van der Mee (2000), Basic relationships for matrices describing scattering by small particles, in *Light Scattering by Nonspherical Particles*, edited by M. I. Mishchenko, J. W. Hovenier, and L. D. Travis, pp. 61–85, Academic, San Diego, Calif.

Hovenier, J. W., H. Volten, O. Muñoz, W. J. van der Zande, and L. B. F. M. Waters (2003), Laboratory studies of scattering matrices for randomly oriented particles: Potentials, problems, and perspectives, *J. Quant. Spectrosc. Radiat. Transfer*, *79–80*, 741–755.

Konert, M., and J. Vandenberghe (1997), Comparison of laser grain size analysis with pipette and sieve analysis: A solution for the underestimation of the clay fraction, *Sedimentology*, *44*, 532–535.

Krotkov, N. A., D. E. Flittner, A. J. Krueger, A. Kostinski, C. Riley, W. Rose, and O. Torres (1999), Effect of particle non-sphericity on satellite monitoring of drifting volcanic ash clouds, *J. Quant. Spectrosc. Radiat. Transfer*, *63*, 613–630.

Lipman, P. W., and D. R. Mullineaux (Eds.) (1981), The 1980 eruptions of Mount St. Helens, Washington, *U.S. Geol. Surv. Prof. Pap.*, *1250*, 844.

Liu, L., M. I. Mishchenko, J. W. Hovenier, H. Volten, and O. Muñoz (2003), Scattering matrix of quartz aerosols: Comparison and synthesis of laboratory and Lorenz-Mie results, *J. Quant. Spectrosc. Radiat. Transfer*, *79–80*, 911–920.

McGimsey, R. G., C. A. Neal, and C. M. Riley (2001), Areal distribution, thickness, mass, volume, and grain size of tephra-fall deposits from the 1992 eruptions of Crater Peak vent, Mt. Spurr Volcano, Alaska, *U.S. Geol. Surv. Open File Rep.*, *OF01-0370*, 38.

Mie, G. (1908), Beiträge zur Optik trüber Medien, speziell kolloidaler Metallösungen, *Ann. Phys.*, *25*, 377–445.

Mishchenko, M. I., L. D. Travis, and A. Macke (1996), Scattering of light by polydisperse, randomly oriented, finite circular cylinders, *App. Opt.*, *35*, 4927–4940.

Mishchenko, M. I., L. D. Travis, R. A. Kahn, and R. A. West (1997), Modeling phase functions for dustlike tropospheric aerosols using a shape mixture of randomly oriented polydisperse spheroids, *J. Geophys. Res.*, *102*, 831–837.

Mishchenko, M. I., W. J. Wiscombe, J. W. Hovenier, and L. D. Travis (2000), Overview of scattering by nonspherical particles, in *Light Scattering by Nonspherical Particles*, edited by M. I. Mishchenko, J. W. Hovenier, and L. D. Travis, pp. 20–60, Academic, San Diego, Calif.

Mishchenko, M. I., L. D. Travis, and A. A. Lacis (Eds.) (2002), *Scattering, Absorption, and Emission of Light by Small Particles*, Cambridge Univ. Press, New York.

Mishchenko, M. I., I. V. Geogdzhayev, L. Liu, J. A. Ogren, A. A. Lacis, W. B. Rossow, J. W. Hovenier, H. Volten, and O. Muñoz (2003), Aerosol retrievals from AVHRR radiances: Effects of particle nonsphericity and absorption and an updated long-term global climatology of aerosol properties, *J. Quant. Spectrosc. Radiat. Transfer*, *79–80*, 953–972.

Muñoz, O., H. Volten, J. F. de Haan, W. Vassen, and J. W. Hovenier (2000), Scattering matrices of olivine and Allende meteorite particles, *Astron. Astrophys.*, *360*, 777–788.

Muñoz, O., H. Volten, J. F. de Haan, W. Vassen, and J. W. Hovenier (2001), Experimental determination of scattering matrices of fly ash and clay particles at 442 and 633 nm, *J. Geophys. Res.*, *106*, 22,833–22,844.

Muñoz, O., H. Volten, J. F. de Haan, W. Vassen, and J. W. Hovenier (2002), Experimental determination of the phase function and degree of linear polarization of El Chichón and Pinatubo volcanic ashes, *J. Geophys. Res.*, *107*(D13), 4174, doi:10.1029/2001JD000983.

Nousiainen, T., and K. Vermeulen (2003), Comparison of measured single-scattering matrix of feldspar particles with T-matrix simulations using spheroids, *J. Quant. Spectrosc. Radiat. Transfer*, *79–80*, 1031–1042.

Nye, C. J., S. E. Swanson, V. F. Avery, and T. P. Miller (1994), Geochemistry of the 1989–1990 eruption of Redoubt Volcano: Part I. Whole rock major and trace element chemistry, *J. Volcanol. Geotherm. Res.*, *62*, 429–452.

Nye, C. J., M. L. Harbin, T. P. Miller, S. E. Swanson, and C. A. Neal (1995), Whole rock major and trace element chemistry of ejecta from Crater Peak, Mount Spurr Volcano, Alaska, *U.S. Geol. Surv. Bull.*, *2139*, 119–128.

Patterson, E. M. (1981), Measurements of the imaginary part of the refractive index between 300 and 700 nanometers for Mount St. Helens ash, *Science*, *211*, 836–838.

Riley, C. M., W. I. Rose, and G. J. S. Bluth (2003), Quantitative shape measurements of distal volcanic ash, *J. Geophys. Res.*, *108*(B10), 2504, doi:10.1029/2001JB000818.

Rose, W. I., and C. A. Chesner (1987), Dispersal of ash in the great Toba eruption, 75,000 years B.P., *Geology*, *15*, 913–917.

Rose, W. I., R. L. Wunderman, M. F. Hoffman, and L. Gale (1983), A volcanologist's review of atmospheric hazards of volcanic activity: Fuego and Mount St. Helens, *J. Volcanol. Geotherm. Res.*, *17*, 133–157.

Rose, W. I., G. J. S. Bluth, D. J. Schneider, G. G. J. Ernst, C. M. Riley, L. J. Enderson, and R. G. McGimsey (2001), Observations of volcanic clouds in their first few days of atmospheric residence: The 1992 eruptions of Crater Peak, Mount Spurr Volcano, Alaska, *J. Geol.*, *109*, 677–694.

Sarna-Wojcicki, A. M., S. Shipley, R. B. Waitt Jr., D. Dzurisin, and S. H. Wood (1981), Areal distribution, thickness, mass, volume, and grain size of air-fall ash from the six major eruptions of 1980, in *The 1980 Eruptions of Mount St. Helens, Washington*, edited by P. W. Lipman and D. R. Mullineaux, *U.S. Geol. Surv. Prof. Pap.*, *1250*, 913–917.

Scott, W. E., and R. G. McGimsey (1994), Character, mass, distribution, and origin of tephra-fall deposits of 1989–1990 eruption of Redoubt Volcano, south-central Alaska, *J. Volcanol. Geotherm. Res.*, *62*, 251–272.

Swanson, S. E., C. J. Nye, T. P. Miller, and V. F. Avery (1994), Geochemistry of the 1989–1990 eruption of Redoubt Volcano: Part II. Evidence from mineral and glass chemistry, *J. Volcanol. Geotherm. Res.*, *62*, 453–468.

Swanson, S. E., M. L. Harbin, and J. R. Riehle (1995), Use of volcanic glass from ash as a monitoring tool: An example from the 1992 eruptions of Crater Peak, Mount Spurr Volcano, Alaska, *U.S. Geol. Surv. Bull.*, *2139*, 129–137.

van de Hulst, H. C. (1957), *Light Scattering by Small Particles*, John Wiley, Hoboken, N. J.

Volten, H., O. Muñoz, E. Rol, J. F. de Haan, W. Vassen, J. W. Hovenier, K. Muinonen, and T. Nousianen (2001), Scattering matrices of mineral aerosol particles at 441.6 nm and 632.8 nm, *J. Geophys. Res.*, *106*, 17,375–17,401.

West, R. A., L. R. Doose, A. M. Eibl, M. G. Tomasko, and M. I. Mishchenko (1997), Laboratory measurements of mineral dust scattering phase function and linear polarization, *J. Geophys. Res.*, *102*, 16,871–16,882.

Williams, H., F. J. Turner, and C. M. Gilbert (1982), *Petrography*, W. H. Freeman, New York.

Winchester, L. W. (1998), Determination of the complex refractive index of samples of volcanic ash, contract report S01394-G, NASA, Washington, D. C.

_____

J. W. Hovenier and L. B. F. M. Waters, Astronomical Institute "Anton Pannekoek," University of Amsterdam, Kruislaan 403, NL-1098 SJ Amsterdam, Netherlands. (hovenier@science.uva.nl; rensw@science.uva.nl)

O. Muñoz, Instituto de Astrofísica de Andalucía (CSIC), Camino Bajo de Húetor 24, E-18080, Granada, Spain. (olga@iaa.es)

W. I. Rose, Department of Geological Engineering and Sciences, Michigan Technological University, Houghton, MI 49931, USA. (raman@mtu.edu)

W. J. van der Zande, B. Veihelmann, and H. Volten, FOM Institute AMOLF, Kruislaan 407, NL-1098 SJ Amsterdam, Netherlands. (w.v.d.zande@amolf.nl; veihelmann@amolf.nl; h.volten@amolf.nl)